Optics and Lasers in Engineering 122 (2019) 1–7

Contents lists available at ScienceDirect

Optics and Lasers in Engineering

journal homepage: www.elsevier.com/locate/optlaseng

Microscopic 3D measurement of shiny surfaces based on a multi-frequency phase-shifting scheme

Yan Hu [a,b], Qian Chen [a], Yichao Liang [a,b], Shijie Feng [a,b], Tianyang Tao [a,b], Chao Zuo [a,b,*]

[a] Jiangsu Key Laboratory of Spectral Imaging & Intelligent Sense, Nanjing University of Science and Technology, Nanjing, Jiangsu Province 210094, China
[b] Smart Computational Imaging (SCI) Laboratory, Nanjing University of Science and Technology, Nanjing, Jiangsu Province 210094, China

ARTICLE INFO

Keywords:
Three-dimensional sensing
Binocular and stereopsis
High dynamic range (HDR)
Optical metrology

ABSTRACT

Microscopic fringe projection profilometry is a powerful 3D measurement technique with a theoretical measurement accuracy better than one micron. However, the defocus of the dense fringe and complex surface reflexivity characteristics usually cause intensity saturation and decrease the fringe quality, which makes the complete 3D reconstruction difficult. To address this problem, we calculate the phase of the highlighted areas from a subset of the phase-shifted fringe images which are not subjected to intensity saturation. A multi-frequency phase-shifting scheme is proposed to improve the integrity of the final phase map of the shiny surface, based on which we can achieve a complete and high-accuracy 3D reconstruction combined with a microscopic telecentric stereo system. Experimental results of different highlight surfaces demonstrate that our approach can retrieve the complete morphology of shiny surfaces with high accuracy and reliability.

1. Introduction

The principle of structured light and triangulation has been widely used in the range of 3D optical metrology applications [1]. Periodic sinusoidal fringe patterns are projected onto an inspected object, and the fringe pattern is distorted by the modulation of the object. To quantitatively calculate the amount of the modulation and reconstruct the 3D result of the target, we need to retrieve the phase value coded in the fringe pattern accurately[2,3]. For now, two commonly used phase retrieval algorithms are Fourier transform based algorithms [4–6] and phase-shifting based algorithms [7–10]. Fourier transform based algorithms are commonly used in dynamic measurement while phase-shifting based algorithms are more suitable for high-accuracy measurement owing to its pixel independently mathematical operational nature. Our recent work has shown that by the phase-based stereo matching method, we can neglect the essential nonlinear response function of the digital projector because the phase errors in different views are automatically balanced out [11]. However, the phase-based stereo matching method is prone to fail when dealing with objects with shiny surfaces. The integrity of the reconstructed model is affected by the highlight regions because we cannot calculate the phase in these areas by dense fringe images.

Shiny surfaces are highly reflective, and thus the light intensity cannot be transformed linearly because of the limited dynamic range of digital cameras. One of the state-of-the-art techniques for this situation is called the high-dynamic range 3D shape measurement [12], which can be classified into two categories: equipment-based techniques and algorithm-based techniques. For the group of the equipment-based techniques, optimal parameters of the equipment, e.g., the exposure time of the camera [13–15] or the projector [16–19] are desired to help capture visible fringe at both shiny and dark areas. Additional optical based methods, e.g., using a polarizer to scan shiny objects have also been investigated [20,21], based on which the polarized highlight intensity can be effectively suppressed. Also, there are hybrid methods by modifying camera exposure, but also taking into account strategies of introducing additional equipment, changing the viewing position, or adjusting parameters of projectors to capture HDR images [22–24]. Based on the maximum intensity modulation, a fast HDR solution employing a high-speed projector to project intensity-varying fringe images at 700 Hz is proposed [25].

For shiny surfaces, however, the problem of saturation may not be readily handled by merely decreasing the exposure time or the intensity of the projected light sometimes. Thus, researchers also developed algorithm-based techniques, which mainly rely on well-designed algorithms to extract phase values from raw fringe images when a free change of the camera or the projector exposure time is not allowed, or additional equipment is not available. Yin et al. [26] suggested measuring shiny surfaces with a single color image. Alternatively, Jiang et al. [27] proposed a real-time HDR 3-D scanning method by projecting additional inverted fringe patterns. Chen et al. [28] found that the

* Corresponding author.
E-mail addresses: chenqian@njust.edu.cn (Q. Chen), zuochao@njust.edu.cn (C. Zuo).

https://doi.org/10.1016/j.optlaseng.2019.05.019
Received 31 December 2018; Received in revised form 18 May 2019; Accepted 18 May 2019
Available online 24 May 2019
0143-8166/© 2019 Elsevier Ltd. All rights reserved.

phase-shifting methods can overcome the image saturation if the number of the phase shift is high enough so we can at least record three unsaturated fringe intensities successfully. Chen et al. [29] proposed a technique by which they also calculate the phase from raw phase-shifting images but without considering whether the images are saturated. Hu et al. [30,31] introduced a phase-shifting based method by taking advantage of no less than three unsaturated fringe image from a standard N-step phase-shifting algorithm.

These related works have successfully addressed HDR measurement problems by various means. However, for microscopic imaging, those shiny parts illuminated by black stripes can no longer be imaged purely black but will be affected by the white stripes because of the short depth of field of the microscopic projection system. In this case, there will be more saturated areas when we use higher frequency fringes. Inspired by the works proposed by Hu et al. [30,31], we propose an HDR measurement method which takes advantage of the generalized phase-shifting algorithm and considers the spatial frequency characteristic of multi-frequency fringe patterns in the microscopic measurement applications. We can calculate the phase values using the standard phase-shifting algorithm when there is no saturation. In those partially saturated areas, we use the generalized phase-shifting algorithm to calculate the wrapped phase. For those over-saturation areas with less than three unsaturated intensities, the phases probably retrievable from lower frequency fringe images are used to fill up the final phase map to increase the measurement integrity. After phase unwrapping and stereo matching of the dual-view telecentric measurement system [11], we can successfully achieve the high-accuracy 3D reconstruction of shiny surfaces (HDR objects). The experiments show that the proposed multi-frequency phase-shifting scheme accommodates the measurements of various kinds of shiny objects with the measurement high-accuracy within one micron.

2. Principals

2.1. Generalized phase-shifting algorithm

Traditional approaches to generate fringe images of fringe projection profilometry involve laser interferometry, physical grating, or slide projector. With recent developments in the area of the digital display, digital projectors have been increasingly applied as the projection units. Based on the controllable phase-shifting amount, the recorded fringe image with δ_n phase-shifting can be expressed by

$$I_n(u,v) = I_0(u,v)\{1 + \alpha(u,v)\cos[\Phi(u,v) + \delta_n], \tag{1}$$

where (u, v) is the pixel coordinate of the camera, I_0 is the average intensity, α is the fringe contrast, Φ is the phase distribution to be measured. δ_n is the shifted reference phase ($n = 1, \ldots, N$). The phase distribution Φ can be calculated independently over no less than three phase-shifted intensities as shown in Fig. 1. Based on minimizing a criterion concerning the difference between ideal intensities and captured intensities [32],

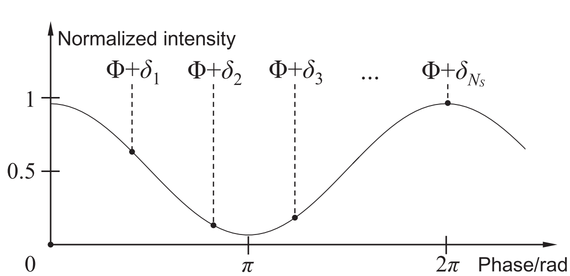

Fig. 1. Sketch map of the relation between the intensity and the shifted phase in a phase-shifting process.

we can obtain the wrapped phase ϕ corresponding to Φ as

$$\phi = -\arctan\left(\frac{\alpha_2}{\alpha_1}\right), \tag{2}$$

with

$$\begin{cases} \alpha_1 = c_{21}\sum_{n=1}^{N} I_n + c_{22}\sum_{n=1}^{N} I_n\cos(\delta_n) + c_{23}\sum_{n=1}^{N} I_n\sin(\delta_n) \\ \alpha_2 = c_{31}\sum_{n=1}^{N} I_n + c_{32}\sum_{n=1}^{N} I_n\cos(\delta_n) + c_{33}\sum_{n=1}^{N} I_n\sin(\delta_n) \end{cases}, \tag{3}$$

and the coefficients $c_{ij,\ i=2,3;\ j=1,2,3}$ in Eq. (3) can be calculated though

$$\mathbf{C} = \begin{bmatrix} c_{11} & c_{12} & c_{13} \\ c_{21} & c_{22} & c_{23} \\ c_{31} & c_{32} & c_{33} \end{bmatrix} = \mathbf{A}^{-1} = \begin{bmatrix} N & \sum_{n=1}^{N}\cos(\delta_n) & \sum_{n=1}^{N}\sin(\delta_n) \\ \sum_{n=1}^{N}\cos(\delta_n) & \sum_{n=1}^{N}\cos^2(\delta_n) & \sum_{n=1}^{N}\sin(\delta_n)\cos(\delta_n) \\ \sum_{n=1}^{N}\sin(\delta_n) & \sum_{n=1}^{N}\sin(\delta_n)\cos(\delta_n) & \sum_{n=1}^{N}\sin^2(\delta_n) \end{bmatrix}^{-1}. \tag{4}$$

Since the phase step δ_n is strictly controlled, two-dimensional wrapped phase distribution $\phi(u, v)$ can be obtained from Eqs. (2)–(4). Particularly, if δ_n is equally divided by an integer N_S in the range $[0, 2\pi)$, Eqs. (2)–(4) can be simplified as the standard phase-shifting algorithm:

$$\phi = -\arctan\left[\frac{\sum_{n=1}^{N_S} I_n\sin(\delta_n)}{\sum_{n=1}^{N_S} I_n\cos(\delta_n)}\right]. \tag{5}$$

2.2. Multi-frequency phase-shifting scheme for HDR surface measurement

The accuracy of the phase values depends on the phase-shifting step number and the fringe contrast. When the final absolute phase is scaled into the same range $[0, 2\pi)$, the phase error variance can be stated as [33].

$$\sigma_\Phi^2 = \frac{2\sigma^2}{N_S f^2 B^2}. \tag{6}$$

Here, σ is the variance of a Gaussian distributed additive noise. N_S is the phase-shifting step number. f is the fringe frequency, indicating the fringe density. B is the fringe modulation. If we have confirmed the phase-shifts, in order to acquire a higher phase accuracy, we should use patterns with higher frequency (f) and try to capture images with better fringe visibility (B) as well.

However, in the projection system, the low depth of field leads to a significantly attenuated fringe contrast when increasing the fringe density. Furthermore, low contrast fringes falling on the shining surface can easily cause intensity saturation. Fig. 2 gives a mathematical model to explain this phenomenon. W_L and W_H are the sinusoidal waves with lower and higher frequency, respectively. Because of the slight defocus, the fringe contrast of W_H with a higher frequency will be smaller than that of W_L. S_1 and S_2 are two saturation thresholds for the surface with

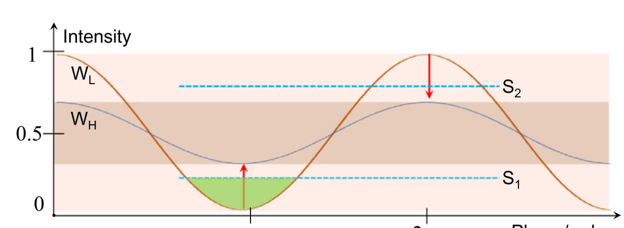

Fig. 2. A illustration of two saturation situations with two sinusoidal waves with different fringe period.

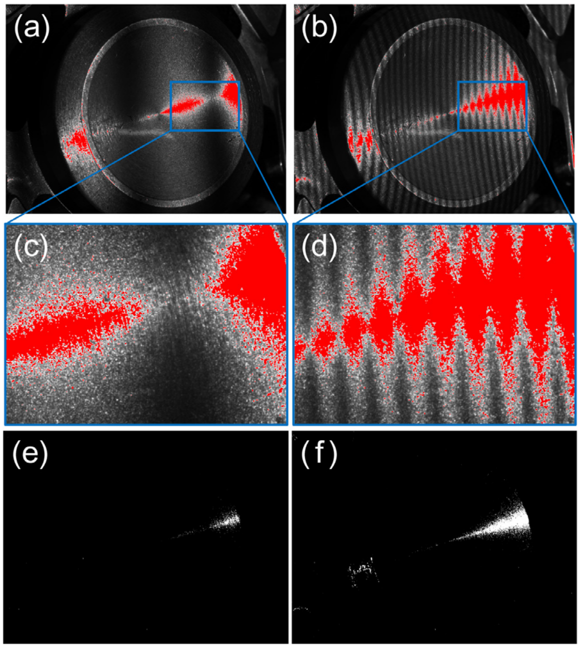

Fig. 3. Comparison of the saturation degree between fringes with different frequency. (a) and (b) Raw fringe images; (c) and (d) Magnified details of saturated parts; (e) and (f) Indexes that show regions with less than three unsaturated intensities.

different reflectivity. The intensities above S_1 or S_2 will cause saturation. For S_1, clearly, all the wave of W_H is above S_1, thus no valid intensities can be recorded. But for W_L, the green area has intensities less than S_1, therefore the phase value can be retrieved by the generalized phase-shifting scheme, which makes the multi-frequency phase-shifting scheme workable. Another situation is that for a surface with saturation threshold of S_2 ($S_2 > S_1$), part of W_L is above S_2 while all the wave of W_H is within the linear intensity range. Then we automatically use W_H for phase calculation since fringe with higher frequency gives more accurate results.

Fig. 3 shows a metal surface covered by fringe patterns with two different frequencies. The periods of the fringe pattern in Fig. 3(a) and (b) are 144 and 12, respectively. Because of the slight defocus caused by the shallow depth of field, the dark stripe in the marked sub-region in Fig. 3(b) is affected by the nearby light because of the convolution of propagating light in space, and thus saturation occurs, as presented in the magnified details in Fig. 3(d). However, when this region is projected by a less dense fringe as shown in Fig. 3(a), the dark stripe gives more unsaturated pixels, as Fig. 3(c) presents, and thus the phase values in such regions can be retrieved. To intuitively show the difference, we extract the region with less than three unsaturated intensities the white areas in Figs. 3(e) and (f) show the pixels with less than three unsaturated intensities. In this kind of area, we cannot calculate the phase because the unknowns are more than the conditions. Correspondingly, Fig. 3(e) has quite fewer pixels where the phase we cannot calculate.

When adjusting the system parameters, we should maintain the saturated region in a small part. It is not appropriate to decrease the exposure time of the whole field only to decrease the saturation area. However, for those samples with a large proportion of saturation, the right way is decreasing the exposure time to leave a small region with saturation. In traditional multi-frequency phase-shifting methods, the fringe patterns with lower frequency are merely used to provide a reference phase map for phase unwrapping, so that the fringe images with the highest frequency determine the final measurement accuracy. Actually, in the saturated regions, the final phase values can be replaced by that derived from the less dense fringe images with less saturated intensities. In this way, we can preserve the 3D reconstruction as complete as possible. For this purpose, we propose a multi-frequency fringe based scheme for HDR surface measurement. Three steps, including image data preparation, saturation detection and compensation algorithms, and phase stereo matching allow the high-accuracy microscopic 3D measurement of shiny surfaces.

Step one is the image data preparation stage, which contains image acquisition, image rectification, and classification according to the fringe frequency. The fringe patterns are sequentially projected with trigger signals for the camera synchronization. **Step two** is the main part corresponding to the proposed multi-frequency fringe based scheme, which is to calculate the unwrapped phase map by three algorithms. Their definitions are detailed in Algorithms 1 , 2 , and 3, respectively.

Algorithm 1: sat_map .

Input: I^m_{set}.
Output: sat_map^m.
for *pixel (u,v)* **do**
  for $i = 1 : N^m_S$ **do**
    jud = the ith intensity at pixel (u, v);
    if $jud \geq sat\_thr$ **then**
      $sat\_map^m(u, v) = sat\_map^m(u, v) + 1$;
    end
  end
end

Algorithm 2: gen_phase_shifting .

Input: I^m_{set}, sat_map^m.
Output: $wrapped \preceq phase \preceq \phi^m$.
for *pixel (u,v)* **do**
  if $sat\_map^m(u, v) = 0$ **then**
    $\phi^m(u, v)$ = Eq. (5).
  else
    $I\_slot = I^{1\sim N_S}_{set}(u, v)$;
    $\delta\_slot = \delta_{1\sim N_S}$;
    $index = (I\_slot \geq sat\_thr)$;
    $I\_slot(index) = empty$;
    $\delta\_slot(index) = empty$;
    if $length(I\_slot) < 3$ **then**
      continue;
    else
      $\phi^m(u, v)$ = Eq. (2);
    end
  end
end

Step three is phase stereo matching and 3D reconstruction, which we will discuss in the next subsection. Table 1 lists the description of the variables used in Step two:

Algorithm 1is to count the number of saturated intensities at each pixel in an image set by **sat_map**. The stored information is to be referenced in the phase unwrapping stage considering the saturation levels of different fringe periods. Algorithm 2 is the phase calculation algorithm for the partially saturated phase-shifting fringe images by **gen_phase_shifting**. We eliminate invalid intensities at each pixel and apply the generalized phase-shifting algorithm corresponding to Eqs. (2)–(4) for the phase calculation. Algorithm 3 is the automatic fusion method for the correctness of the unwrapped phase by **multi_freq_hdr**. As shown in Fig. 3(e) and (f), because of the defocus of the projected pattern, the denser fringes are easier to be blurred, and thus there will be fewer pixels with no less than three valid intensities.

Table 1
Parameters used to calculate phase maps.

Items	description
I_{set}^{m}	the mth fringe image set containing a group of standard phase-shifted fringe images.
M	the total number of the fringe image sets.
sat_map^{m}	the pixel-wise map containing the saturated intensity number of I_{set}^{m}.
N_S^m	the phase-shifting number of the mth image set.
per^m	the fringe period corresponding to the mth image set.
Φ_{eq}^{m}	equivalent unwrapped phase map of Φ^m.
k^m	the fringe order for phase unwrapping.
sat_thr	the saturation threshold intensity.
I_slot	a temporary storage for the unsaturated I_n in a phase-shifting process.
δ_slot	a temporary storage for δ_n of unsaturated intensities I_n.
δ_{std}	an array containing the standard phase-shifts.
ind^m	a two-dimensional index map, in which '1' indicates over-saturation.
$\sim ind^m$	the unary complement of ind^m.
ind_rep^m	an index map storing which pixels in Φ are to be replaced by Φ_{eq}^{m}.

Algorithm 3: multi_freq_hdr .

Input: $sat\_map^{1\sim M}$, $\phi^{1\sim M}$, k^m.
Output: $Unwrapped{\preceq}phase{\preceq}\Phi$.

$\Phi^1 = \phi^1$;
for $m = 2 : M$ **do**
  $k^m = \mathrm{round}[(\Phi^{m-1} \cdot per^{m-1}/per^m - \phi^m)/2\pi]$;
  $\Phi^m = \phi^m + 2\pi k^m$;
end
for $m = 1 : M$ **do**
  $\Phi_{eq}^m = \Phi^m \cdot per^m/per^M$;
end
for $m = 1 : M$ **do**
  $ind^m = sat\_map^m > (N_S - 3)$;
end
for $m = 1 : M$ **do**
  $ind\_rep^m = ind^M{\preceq}\&{\preceq}ind^{(M-1)}{\preceq}\ldots{\preceq}\& \sim ind^m$;
end
for $m = 1 : M$ **do**
  $\Phi(ind\_rep^m) = \Phi_{eq}^m(ind\_rep^m)$;
end

For these pixels, we use the equivalent phase derived from the less dense fringe set to fill up the unwrapped phase map. This algorithm searches the phase candidates from the relatively denser image set and then the looser ones for better noise immunity.

To make it easier to understand the whole process of the proposed scheme, we draw a flowchart containing the three steps as shown in Fig. 4, in which we measured a screw thread as the example.

2.3. 3D Reconstruction based on phase stereo matching

The structure model of our measurement system is presented in Fig. 5(a). Sinusoidal patterns encoded with horizontally increased phase maps are projected in sequence from the digital projector. The fringes are deformed by the object and then captured by two telecentric cameras. The camera model is acA2040-120um with the pixel size of 3.45 μm, and resolution of 2048 × 1536. The model of the telecentric lens is XF-UTL-0296X175 with a magnification of 0.296 ×, depth of field of 16.1 mm, and spatial resolution of 31.2μm. Thus the measurable volume in the object side is about 23.87 mm × 17.9 mm × 16.1 mm, which satisfies our goal in microscopic 3D measurements.

Based on the discrete nature of the digital projector, the fringe period cannot be reduced indefinitely. To make the phase-shifting process compatible with the spatial distribution of the fringe variation, we set the fringe period as 12 pixels which are also the number of the phase-shifting. Because all sets of the fringe patterns with a different period contributes part of the phase value in the final phase map, the phase-shifting steps of different fringe periods are all the same. The phase-shifting step depends on the memory capacity of the projector. To balance the measurement speed and accuracy, we use 48 patterns in total to maximize the use ratio of the memory. The period ratio between the neighbored periods is less than 6.4 to minimize the phase unwrapping errors. Although we use 48 patterns in one measurement, actually only 1.2 is used to finish the data acquisition because the exposure time of both the projector and cameras are strictly synchronized. The parameters used in the experiments are as follows, M is 4, $N_S^{1\sim 4}$ are [12 12 12 12], and $Per_S^{1\sim 4}$ are [912 144 24 12]. By using the proposed multi-frequency fringe based method, the absolute phase value Φ from both cameras can be obtained for the stereo matching.

Telecentric epipolar rectification of the fringe images is carried out first. Without loss of generality, we consider the left camera as the main camera. As Fig. 5(b) shows, for a pixel (u_L, v_L) on the left camera with phase value $\Phi(u_L, v_L)$, the task is to find the corresponding pixel u_R in the v_Lth row on the right image. Because the fringe direction is vertical so that the unwrapped phase value increases along the horizontal direction. We first obtain the integral pixel u_R^I that has the nearest phase value to $\Phi(u_L, v_L)$ in the v_Lth row with its phase being $\Phi(u_R^I)$. Then sub-pixel coordinate u_R is thereby calculated based on inverse linear interpolation:

$$u_R = u_R^I + \begin{cases} \dfrac{\Phi(u_L, v_L) - \Phi(u_R^I)}{\Phi(u_R^I + 1) - \Phi(u_R^I)}, \Phi(u_L, v_L) > \Phi(u_R^I) \\ \dfrac{\Phi(u_L, v_L) - \Phi(u_R^I)}{\Phi(u_R^I) - \Phi(u_R^I - 1)}, \Phi(u_L, v_L) \le \Phi(u_R^I) \end{cases} \tag{7}$$

After completing the left-right consistency check in the stereo matching, we have the matched pixel pairs. For more accurate sub-pixel searching, u_R can be interpolated with a more complex fitting method that involves more neighboring pixels, but this will cost more time. Together with the new camera parameters after the epipolar rectification, we can directly derive the point cloud data [11]. As we know that the 3D data is obtained based on the homologous points matching from multi-views. In our system, the multi-view refers to two telecentric cameras. Since the stereo matching work only relies on the monotonous phase maps from two calibrated and rectified cameras, we no longer need to calibrate the projector because the two cameras have already provided the viewing angles for the 3D measurement.

3. Experiments

3.1. Comparison with traditional multi-frequency method

Phase-shifting algorithms assume that the captured intensities vary in the form of a sinusoidal wave as the phase shifts linearly. If the sample

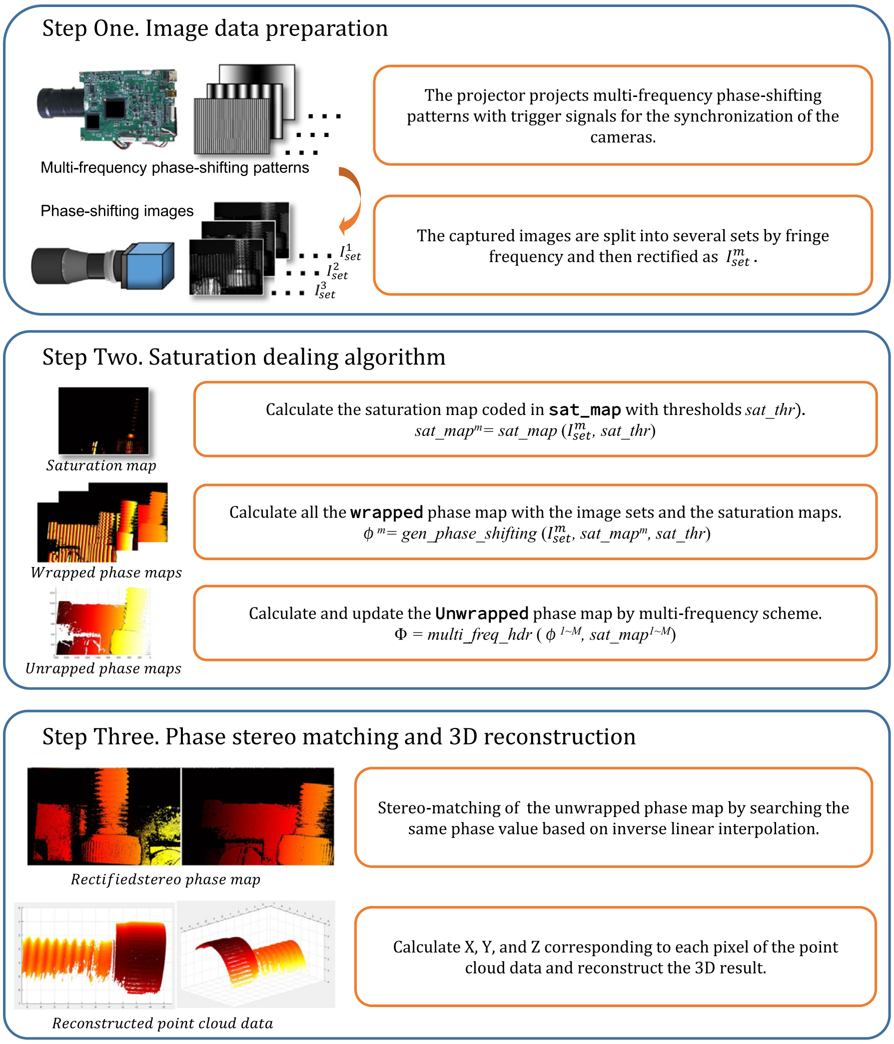

Fig. 4. The flowchart of the proposed algorithm for shiny surface measurement.

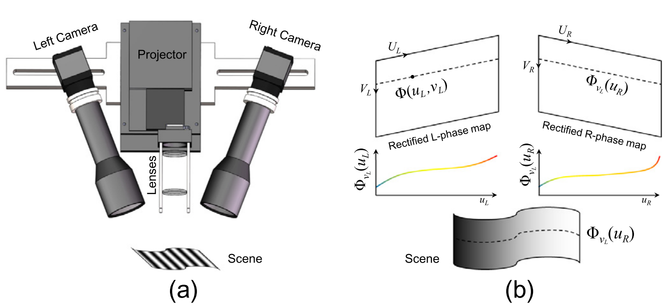

Fig. 5. (a) Simplified structure model of the system; (b) Illustration of the binocular matching based on the unwrapped phase map.

is very reflective, a portion of saturated intensities (255 if the image sampling resolution is 8 bit) will replace those intensities larger than the maximum of the sampling limit, which is defined as partial saturation. To compare our proposed method with the traditional multi-frequency method when dealing with partially saturated targets, we conducted measurements of two samples with a shiny surface.

Fig. 6 presents the measurement results. The first sample is a stamped logo on a metal watch strap. As shown in Fig. 6(a), the shiny surface is imaged with quite severe saturation around the letters when projected by fringes. The other sample in Fig. 6(e) is a printed circuit board with metal bonding pads and white silkscreen letters and lines. If we apply the traditional phase-shifting algorithm using these saturated intensities for the phase calculation, we will incorrectly reconstruct the saturated regions on the samples, as shown in Fig. 6(b) and (f). Ripples appear in those partially or totally saturated regions. For those regions with unsaturated intensity number less than three, we, however, can no longer retrieve the phase value, which causes incomplete results, as shown in Fig. 6(c) and (g). By using our proposed multi-frequency fringe based method, we can anyhow acquire a phase map as complete as possible with correct phase values, and the 3D surface profile of the shiny samples can thus be reconstructed as well, as shown in Fig. 6(d) and (h).

We still preferred denser fringe though they give lower fringe contrast because of their high immunity to noise, as Eq. (6) manifests. Note that the success of the proposed method is under a necessary condition, that is, the method should be used in a microscopic 3D measurement system because it is the low depth of field of the microscopic projection system that makes the denser fringe easily defocused. For the measurement system for relatively large scale objects, the field of view of the optical system will be quite bigger, and the depth of field is much deeper. Thus the fringe contrast nearly keeps unchanged, in which case our method may no longer be valid.

3.2. Measurement of shiny samples

To demonstrate the performance of the proposed method for microscopic measurement of shiny surfaces, we conducted two experiments on metal samples. The first example is a nickel-plated plate from a

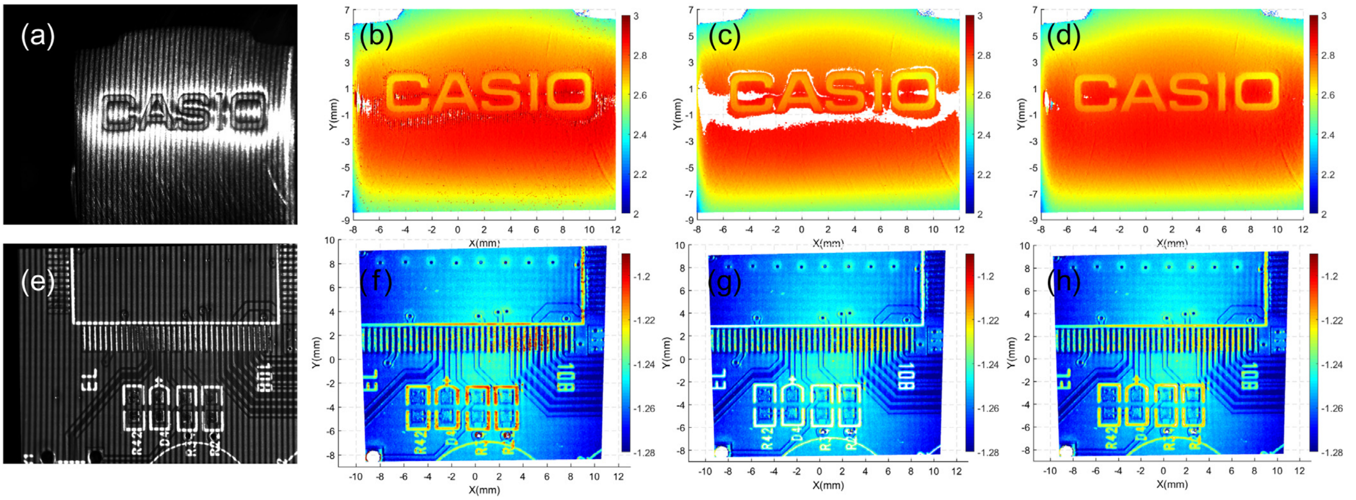

Fig. 6. Comparison of our method and the traditional method when dealing with partially saturated targets. (a) Fringe image of a stamped logo on a metal watch strap; (e) Fringe image of a printed circuit board; (b) and (f) Results with error and ripples; (c) and (g) Results with error-contained regions eliminated; (d) and (h) Results from our proposed multi-frequency fringe based method for HDR surface.

mechanical watch, as shown in Fig. 7(a). We measured both sides, and the fringe images from the right camera are presented in Fig. 7(b) and (c), respectively. Because of the high reflection of the metal surface and the weak depth of field of the projected fringe, saturated regions are conspicuous. By the processes as drawn in the flowchart in Fig. 7, we can finally get the absolute 3D point cloud data. Fig. 7(d) is the reconstructed 3D model of the bottom side. Fig. 7(e) is the reconstructed 3D model of the top side. Fig. 7(d_1)–(d_3) are three sectional views of the data as the lines labeled in Fig. 7(d). Fig. 7(e_1)–(e_3) are three sectional views of the data as the lines labeled in Fig. 7(e). These section views provide a more intuitive vision to check the height information on the surface. As known that the measured plate is used for mounting and fixing gear bearings in a mechanical watch, thus an irregularly manufactured plate will invalidate the normal function of a watch. From Fig. 7(d) and (e), we can expediently check the coplanarity and height difference between planes, which provides an efficient way for quality control on the production line.

In the other experiment, the measured targets are two steel gaskets, as shown in Fig. 8(a). The top one has not been used to bear force, and it remains in its original shape, while the other one has gotten a circle-shaped indentation after being used to decrease the pressure on

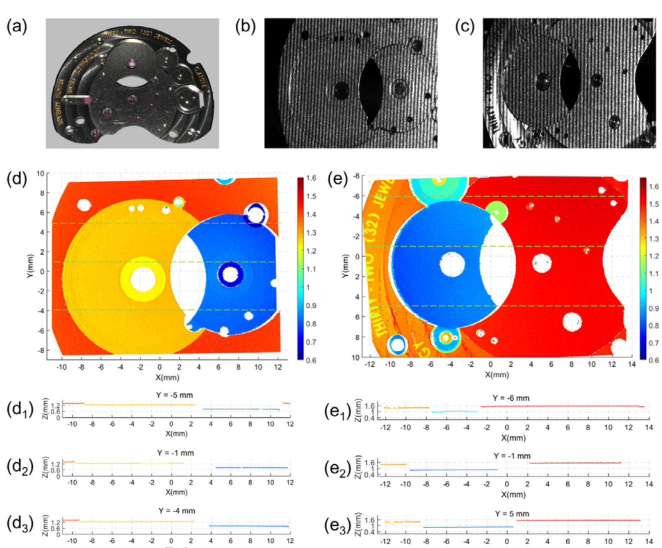

Fig. 7. Experiments on a nickel-plated plate of a mechanical watch. (a) Sample image; (b) A fringe image of the bottom side; (c) A fringe image of the top side; (d) The reconstructed 3D model of the bottom side; (e) The reconstructed 3D model of the top side; (d_1)–(d_3) Sectional views of the data as the lines labeled in (d); (e_1)–(e_3) Sectional views of the data as the lines labeled in (e).

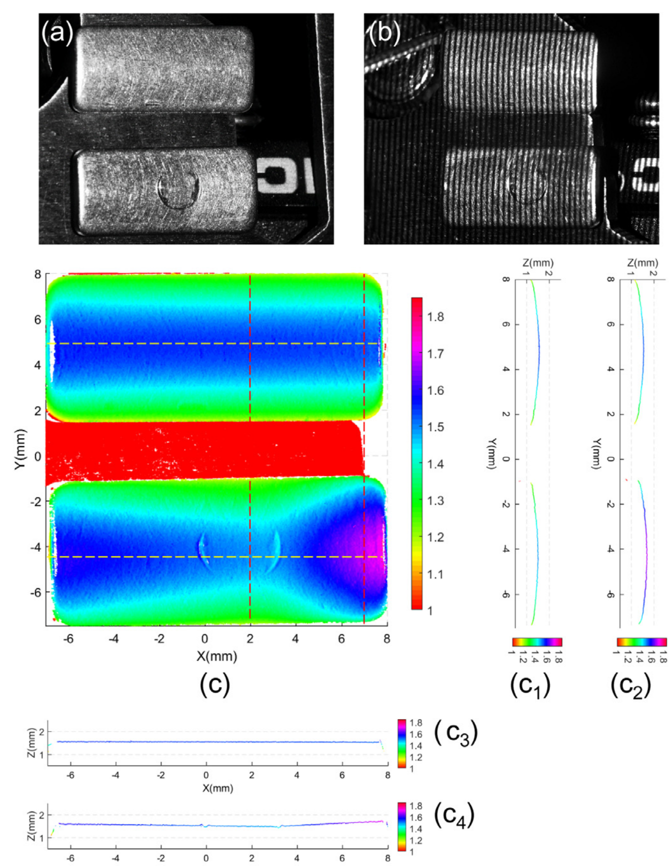

Fig. 8. Experiments on the deformation measurement of two steel gaskets. (a) Sample image; (b) One of the fringe image; (c) Top view of the reconstructed 3D model; (c_1) and (c_2) Sectional views of the data as the red lines labeled in (c); (c_3) and (c_4) Sectional views of the data as the yellow lines labeled in (c).

the contacted surface, which can be seen in Fig. 8(a). The measurement is to analyze the deformation of the gasket and provide quantitative information about the profile at the same time. Fig. 8(b) is one of the fringe images that suffer from saturation. After the same process as used in the last experiment, the absolute 3D point cloud data is obtained as shown in Fig. 8(c), from which we can find that the shape of the bottom gasket has been different from the top one. The indentation can be easily found from the color-coded 3D result. Due to the pressure from the weight, it is lower in the middle part while higher at both ends. Fig. 8(d) and (e) are two vertical sections corresponding to the red dashed lines in Fig. 8(c). Fig. 8(f) and (g) are two horizontal sections corresponding to the yellow dashed lines in Fig. 8(c). From these section views, the quantitative shape deformation of the samples can be easily acquired and used for analysis.

4. Conclusion

In this paper, we present a microscopic 3D measurement of shiny targets based on a multi-frequency phase-shifting scheme. At each pixel, only the unsaturated intensities are used to calculate the phase, and the phase unwrapping process is updated by our proposed method. Because of the low depth of field in the projection light path, denser fringe patterns are easier to be defocused, and thus the integrity of the 3D result is seriously influenced. Our method tries to replace the unavailable phase at the severely saturated regions by the phase calculated from less dense fringe images. However, when dealing with those regions with constant saturation during phase-shifting, we cannot acquire useful phases even using low-frequency fringe patterns.

The overall process of the proposed method is detailed, and the flowchart of the whole procedure is provided. The experimental results show that our method can be successfully applied in industrial applications, such as quality control and on-line inspection for micro-scale products with shiny surfaces. Though the depth of field of the telecentric cameras is enough to measure samples within several millimeters, an excellent solution to increase the measurable volume is using Scheimpflug principle to make the cameras have a bigger common field of view [34]. However, the calibration of the system will become more complicated since a tilt transformation needs to be added to the imaging modeling. The future work is to analyze further how the density and phase-shifting step affects the phase accuracy when different degrees of saturation happens.

Acknowledgments

National Key R & D Program of China (2017YFF0106403), National Natural Science Foundation of China (61722506, 61705105, 111574152), Final Assembly "13th Five-Year Plan" Advanced Research Project of China (30102070102), Equipment Advanced Research Fund of China (61404150202), The Key Research and Development Program of Jiangsu Province, China (BE2017162), Outstanding Youth Foundation of Jiangsu Province of China (BK20170034), National Defense Science and Technology Foundation of China (0106173), Six Talent Peaks project of Jiangsu Province, China (2015-DZXX-009), 333 Engineering Research Project of Jiangsu Province, China (BRA2016407), Fundamental Research Funds for the Central Universities (30917011204, 30916011322), Open Research Fund of Jiangsu Key Laboratory of Spectral Imaging & Intelligent Sense (3091601410414), China Postdoctoral Science Foundation (2017M621747), Jiangsu Planned Projects for Postdoctoral Research Funds (1701038A).

References

[1] Lazaros N. Review of stereo vision algorithms: from software to hardware. Int J Optomechatronics 2008;2(4):435–62. doi:10.1080/15599610802438680.
[2] Pan B, Kemao Q, Huang L, Asundi A. Phase error analysis and compensation for nonsinusoidal waveforms in phase-shifting digital fringe projection profilometry. Opt Lett 2009;34(4):416–18.
[3] Feng S, Chen Q, Gu G, Tao T, Zhang L, Hu Y, et al. Fringe pattern analysis using deep learning. Adv Photon 2019;1(2):1–7–7. doi:10.1117/1.AP.1.2.025001.
[4] Su X, Zhang Q. Dynamic 3-d shape measurement method: a review. Opt Lasers Eng 2010;48(2):191–204.
[5] Zuo C, Tao T, Feng S, Huang L, Asundi A, Chen Q. Micro fourier transform profilometry (μftp): 3d shape measurement at 10,000 frames per second. Opt Lasers Eng 2018;102:70–91.
[6] Hu Y, Chen Q, Zhang Y, Feng S, Tao T, Li H, et al. Dynamic microscopic 3d shape measurement based on marker-embedded fourier transform profilometry. Appl Opt 2018;57(4):772–80.
[7] Zuo C, Chen Q, Gu G, Feng S, Feng F, Li R, et al. High-speed three-dimensional shape measurement for dynamic scenes using bi-frequency tripolar pulse-width-modulation fringe projection. Opt Lasers Eng 2013;51(8):953–60.
[8] Zuo C, Feng S, Huang L, Tao T, Yin W, Chen Q. Phase shifting algorithms for fringe projection profilometry: a review. Opt Lasers Eng 2018;109:23–59.
[9] Feng S, Zuo C, Tao T, Hu Y, Zhang M, Chen Q, et al. Robust dynamic 3-d measurements with motion-compensated phase-shifting profilometry. Opt Lasers Eng 2018;103:127–38.
[10] Hu Y, Chen Q, Tao T, Li H, Zuo C. Absolute three-dimensional micro surface profile measurement based on a greenough-type stereomicroscope. Meas Sci Technol 2017;28(4):045004.
[11] Hu Y, Chen Q, Feng S, Tao T, Asundi A, Zuo C. A new microscopic telecentric stereo vision system-calibration, rectification, and three-dimensional reconstruction. Opt Lasers Eng 2019;113:14–22.
[12] Feng S, Zhang L, Zuo C, Tao T, Chen Q, Gu G. High dynamic range 3-d measurements with fringe projection profilometry: a review. Meas Sci Technol 2018.
[13] Zhang S, Yau S-T. High dynamic range scanning technique. Opt Eng 2009;48(3):033604.
[14] Ekstrand L, Zhang S. Autoexposure for three-dimensional shape measurement using a digital-light-processing projector. Opt Eng 2011;50(12):123603.
[15] Zhong K, Li Z, Zhou X, Li Y, Shi Y, Wang C. Enhanced phase measurement profilometry for industrial 3d inspection automation. Int J Adv Manuf Technol 2015;76(9–12):1563–74.
[16] Waddington C, Kofman J. Saturation avoidance by adaptive fringe projection in phase-shifting 3d surface-shape measurement. In: Optomechatronic technologies (ISOT), 2010 international symposium on. IEEE; 2010. p. 1–4.
[17] Babaie G, Abolbashari M, Farahi F. Dynamics range enhancement in digital fringe projection technique. Precis Eng 2015;39:243–51.
[18] Li D, Kofman J. Adaptive fringe-pattern projection for image saturation avoidance in 3d surface-shape measurement. Opt Express 2014;22(8):9887–901.
[19] Lin H, Gao J, Mei Q, He Y, Liu J, Wang X. Adaptive digital fringe projection technique for high dynamic range three-dimensional shape measurement. Opt Express 2016;24(7):7703–18.
[20] Chen T, Lensch HP, Fuchs C, Seidel H-P. Polarization and phase-shifting for 3d scanning of translucent objects. In: 2007 IEEE conference on computer vision and pattern recognition. IEEE; 2007. p. 1–8.
[21] Salahieh B, Chen Z, Rodriguez JJ, Liang R. Multi-polarization fringe projection imaging for high dynamic range objects. Opt Express 2014;22(8):10064–71.
[22] Feng S, Zhang Y, Chen Q, Zuo C, Li R, Shen G. General solution for high dynamic range three-dimensional shape measurement using the fringe projection technique. Opt Lasers Eng 2014;59:56–71.
[23] Liu G-h, Liu X-Y, Feng Q-Y. 3D shape measurement of objects with high dynamic range of surface reflectivity. Appl Opt 2011;50(23):4557–65.
[24] Jiang H, Zhao H, Li X. High dynamic range fringe acquisition: a novel 3-d scanning technique for high-reflective surfaces. Opt Lasers Eng 2012;50(10):1484–93.
[25] Zhao H, Liang X, Diao X, Jiang H. Rapid in-situ 3d measurement of shiny object based on fast and high dynamic range digital fringe projector. Opt Lasers Eng 2014;54:170–4.
[26] Yin Y, Cai Z, Jiang H, Meng X, Xi J, Peng X. High dynamic range imaging for fringe projection profilometry with single-shot raw data of the color camera. Opt Lasers Eng 2017;89:138–44.
[27] Jiang C, Bell T, Zhang S. High dynamic range real-time 3d shape measurement. Opt Express 2016;24(7):7337–46.
[28] Chen Y, He Y, Hu E. Phase deviation analysis and phase retrieval for partial intensity saturation in phase-shifting projected fringe profilometry. Opt Commun 2008;281(11):3087–90.
[29] Chen B, Zhang S. High-quality 3d shape measurement using saturated fringe patterns. Opt Lasers Eng 2016;87:83–9.
[30] Hu E, He Y, Chen Y. Study on a novel phase-recovering algorithm for partial intensity saturation in digital projection grating phase-shifting profilometry. Optik-Int J Light Electron Opt 2010;121(1):23–8.
[31] Hu E, He Y, Wu W. Further study of the phase-recovering algorithm for saturated fringe patterns with a larger saturation coefficient in the projection grating phase-shifting profilometry. Optik-Int J Light Electron Opt 2010;121(14):1290–4.
[32] Lai G, Yatagai T. Generalized phase-shifting interferometry. JOSA A 1991;8(5):822–7.
[33] Zuo C, Huang L, Zhang M, Chen Q, Asundi A. Temporal phase unwrapping algorithms for fringe projection profilometry: a comparative review. Opt Lasers Eng 2016;85:84–103.
[34] Peng J, Wang M, Deng D, Liu X, Yin Y, Peng X. Distortion correction for microscopic fringe projection system with Scheimpflug telecentric lens. Appl Opt 2015;54(34):10055–62.